

Large-eddy simulation of the planetary boundary layer under baroclinic conditions during daytime and sunset turbulence

Umberto Rizza,^{a,*} Mario M. Miglietta,^{a,b} Otávio C. Acevedo,^c Vagner Anabor,^c Gervasio A. Degrazia,^c Antonio G. Goulart^d and Hans R. Zimmerman^c

^a ISAC-CNR, Istituto di Scienze dell'Atmosfera e del Clima, Dipartimento Terra e Ambiente, Consiglio Nazionale delle Ricerche, Lecce, Italy

^b ISE-CNR, Istituto per lo Studio degli Ecosistemi, Dipartimento Terra e Ambiente, Consiglio Nazionale delle Ricerche, Pallanza, Italy

^c UFSM, Universidade Federal de Santa Maria, Departamento de Física, Santa Maria, Brazil

^d UNIPAMPA, Universidade Federal do Pampa, Departamento de Tecnologia, Alegrete, Brazil

ABSTRACT: This study investigates the Large-Eddy Simulation (LES) technique in the diurnally varying atmospheric boundary layer in conditions of realistic environmental forcing. The initial settings of meteorological fields are obtained by 'ingesting' into the LES domain the vertical profiles of wind, temperature and specific humidity provided by the meteorological model WRF. The surface values of potential temperature and specific humidity from the WRF simulation are used as forcing parameters for the LES runs. These forcing parameters are updated during the runs every 1 h. A methodology is developed to derive the components of the geostrophic wind profile that is used in LES to model the large-scale horizontal mean pressure gradient and treated as an external forcing. This methodology involves the meteorological model WRF. In this context, the WRF model has a dual task: (1) providing realistic atmospheric environmental forcings to LES and (2) providing a very large dataset to investigate possible improvements of the LES setting to make the numerical prediction more realistic.

The principal results obtained by the present study is that the use of geostrophic wind shear profiles improves the prognostic capability of LES in reproducing the wind field pattern in the planetary boundary layer, this is an important parameter for the proper description of the decay of the turbulent kinetic energy at sunset. Copyright © 2012 Royal Meteorological Society

KEY WORDS Large-eddy simulation; planetary boundary layer; baroclinic boundary layer; turbulence decay

Received 17 June 2011; Revised 12 October 2011; Accepted 21 October 2011

1. Introduction

Large-Eddy Simulation (LES) is an established technique that has been extensively used to study idealized turbulent flows. A usual application concerns the planetary boundary layer (PBL) under a wide range of stability conditions. In this context, following the initial works of Deardorff (1970, 1972, 1980) there have been several and successful investigations using LES of the daytime convective boundary layer that is typically well mixed and driven by a combination of buoyancy and shear (Moeng, 1984; Mason, 1989; Nieuwstadt *et al.*, 1992; Sullivan *et al.*, 1998; Stevens *et al.*, 1999).

At the end of the afternoon, when the surface heat fluxes begin to decrease sharply, and the turbulent kinetic energy begins to decay, the daytime PBL turns from a convective well-mixed layer to a stable nocturnal PBL. It is characterized by an intermittently turbulent residual layer overlying a stably stratified boundary layer. Under stable conditions the typical size of eddies becomes of the order of a few metres, imposing an additional burden on the sub-filter scale modelling. The investigation of the evening transition and the stably stratified

atmosphere with LES is in general more challenging than the study of the convective boundary layer (CBL), and there have been less studies related to this topic (Nieuwstadt and Brost, 1986; Mason and Thomson, 1987; Andren *et al.*, 1994; Brown *et al.*, 1994; Kosovic, 1997; Porté-Agel *et al.*, 2000; Saiki *et al.*, 2000; Acevedo and Fitzjarrald, 2001; Beare *et al.*, 2006; Anderson *et al.*, 2007).

The mid-latitude PBL over land often has a significant diurnal cycle, which is comprised of all these turbulent regimes. Its description with LES is still a huge computational task because it demands an extremely large number of computational grid points (10^7 – 10^9) and a large number of time steps ($\sim 10^5$). Related to this topic, mention can be made of the recent work from Basu *et al.* (2008) who were able to describe one full day of the Wangara (Clarke *et al.*, 1971) experimental data set using a dynamical subgrid-scale model.

Parameters of the ambient atmosphere in LES studies conducted so far were typically prescribed in an idealized form. In most of these applications, LES was used as a tool to evaluate the different physical mechanisms that determine the PBL turbulent structures. The studies of Pino *et al.* (2003), Beare *et al.* (2006), Conzemius and Fedorovich (2007) and Basu *et al.* (2008) have provided important, although a limited, quantity of information about the abilities of LES to handle real PBL flows coupled with the changing ambient atmosphere. To provide suitable data under the wide range of the PBL weather conditions,

* Correspondence to: U. Rizza, ISAC-CNR, Istituto di Scienze dell'Atmosfera e del Clima, Consiglio Nazionale delle Ricerche, Strada Provinciale Lecce Monteroni, km.1.2, 73100, Lecce, Italy.
E-mail: u.rizza@isac.cnr.it

the LES should be able to reproduce the PBL turbulence dynamics with the proper actual external forcing adequately. Two approaches dealing with this problem are: (1) the use of multiple nested grids within a mesoscale weather numerical model coupled with LES in a two-way configuration (Moeng *et al.*, 2007) or (2) representing the atmospheric forcing processes having a scale larger than the LES domain with additional terms in the LES equations (Conzemi, 2004).

One aspect that has not adequately been investigated with LES is the baroclinicity, which in the lower atmosphere is a rule rather than the exception (Arya and Wyngaard, 1975). Until now, almost invariably, most LES studies have used geostrophic winds that are constant with height that is the geostrophic wind shear has not been considered so far. The assumption of a barotropic PBL appears to be an oversimplification even in the case of quiescent synoptic situations (Beare *et al.*, 2006). In this context, mention can also be made of the work of Brown (1996, 1999), who considered the geostrophic shear as an external parameter in a series of neutral/convective LES runs. This was equivalent to assuming positive/negative geostrophic shear with no heat advection. This is the simplest case of baroclinicity that does not require modification of the LES equations. Again imposing the geostrophic shear as an external parameter, Zilitinkevich and Esau (2003) used LES to investigate the effects of baroclinicity in the estimation of the PBL depth under neutral conditions. Other forms of baroclinicity require the adaptation of model equation for the potential temperature allowing for advection of the mean temperature gradient (Sorbján, 2004).

The primary goal of this study is to perform LES of the PBL considering realistic environmental atmospheric settings. In this context, different initialization methods may be used depending on whether one uses: (1) local surface observational data and soundings, (2) a mesoscale meteorological model, or, (3) a composite method as a combination of the previous two. Considering the difficulty in gathering observational data from atmospheric soundings, the use of a mesoscale model may be helpful in many aspects. It allows, for example, the implementation of a numerical procedure providing adjustment (nudging) of the simulated CBL mean flow fields to the evolving larger scale external flow fields (Scipion *et al.*, 2009). This makes the employed LES code capable of reproducing a wider range of CBL conditions associated with different environmental forcing.

This task will be realized by the NCAR-LES (Moeng, 1984; Sullivan *et al.*, 1994) model with the mesoscale model Weather Research and Forecasting (WRF, <http://www.wrf-model.org/index.php>) This coupling will be accomplished by putting the LES domain that has a horizontal extension of few kilometres, around a specified point of the WRF inner grid. The initial profiles of temperature, specific humidity and the components of the wind are then obtained 'ingesting' the corresponding vertical profiles of the same variables extracted from the specified point of the WRF grid into the LES domain.

The surface values of potential temperature and specific humidity from the WRF simulation are used as forcing parameters for the LES. Additionally, the large-scale horizontal pressure gradient that is needed to calculate the geostrophic wind is determined from the isobaric geopotential heights calculated within the outer WRF grid. These profiles are specified at the model initialization time, and are updated during the LES runs.

The second major goal is to investigate the effects of the baroclinic setup in the LES study of a daytime and sunset PBL. In the PBL, the baroclinicity can considerably modify the

thermal structure due to advection of cold or warm air, and also turbulence and mixing, due to the baroclinic shear (Sorbján, 2004). The geostrophic shear or baroclinicity is related to temperature gradients through the well-known 'thermal wind' equations (Arya and Wyngaard, 1975) and consequently it would require the adaptation of model equations in order to incorporate the thermal advection, with adjustment for the effects of buoyancy (Sorbján, 2004). This modification would provide non-uniform heating or cooling as the mean wind is function of height. Nevertheless, it has been demonstrated (Brown, 1996) that in convective conditions the effect of such a modification was not significant. Having this work focused on the diurnal convective hours, we follow the approach of Brown (1996) according to which only the geostrophic shear will be provided at any instant of time without modifying the equation for the virtual potential temperature.

We show that, using this approach, LES has the potential to simulate more realistic cases. This methodology will possibly have important applications in any meteorological phenomenon in which the knowledge of the unsteady turbulent flows with high spatial and temporal resolution is required, e.g. in the field of wind energy and wind shear.

2. The WRF mesoscale simulation and synoptic conditions

The Weather Research and Forecasting (WRF) Model is a numerical weather prediction system that features multiple dynamical cores and a three-dimensional variational data assimilation system. WRF is suitable for a broad spectrum of applications across scales ranging from metres to thousands of kilometres (<http://www.wrf-model.org/index.php>).

WRF offers multiple physics options that can be combined in many different ways considering the specific problem that is being investigated. Table 1 shows the Land-Surface and Planetary Boundary Layer physics options that have been chosen for the present study. It is important to mention that, when a PBL scheme is activated in WRF, then a specific vertical diffusion scheme is de-activated with the assumption that the PBL scheme will handle this process. For this study the Mellor-Yamada-Janjić (MYJ) PBL scheme (Janjić, 2001), and the Noah land-surface model (LSM) (Chen and Dudhia, 2001) have been used. The MYJ PBL scheme derives the eddy diffusivities coefficients and the boundary layer height from the estimations of the turbulent kinetic energy, which is calculated from the Mellor-Yamada 2.5 turbulence closure model (Mellor and Yamada, 1982) through the full range of atmospheric turbulent regimes.

In Figure 1 the localization of two grids used for the WRF mesoscale simulation is depicted. The outer grid that has an area of 2000×2000 km and a horizontal grid spacing of 20×20 km. It includes the southern regions of Brazil, Uruguay and parts of Paraguay and Argentina. The inner grid is centred at $(-31.40, -53.70)$, close to the city of Candiota (denoted in Figure 1 by a 'X') in the border between southern Brazil and Uruguay. The aspect ratio of the horizontal resolution of the two grids is 4:1. The details of the two grids are summarized in Table 2. The lateral conditions to WRF are provided by the NCEP Final Analysis (FNL from GFS, ds083.2) with 1° resolution, prepared operationally every 6 h.

The Candiota site is close to a major electric power plant, and was chosen because there are meteorological facilities collecting experimental data. Micrometeorological campaigns have been carried out there during the different seasons

Table 1. Weather research and forecasting (WRF) model setup: physics and land surface parameters.

WRF input name		Description
sf_sfclay_physics	2	Monin-Obukhov (Janjić Eta) scheme
sf_surface_physics	2	Unified Noah land-surface model
bl_pbl_physics	2	Mellor-Yamada- Janjić scheme: Eta operational scheme. One-dimensional prognostic turbulent kinetic energy scheme with local vertical mixing
Isfflx	1	heat and moisture fluxes from the surface
diff_opt	1	Full diffusion: Gradients use full metric terms to more accurately compute horizontal gradients in sloped coordinates
km_opt	4	The vertical diffusion is assumed to be done by the PBL scheme

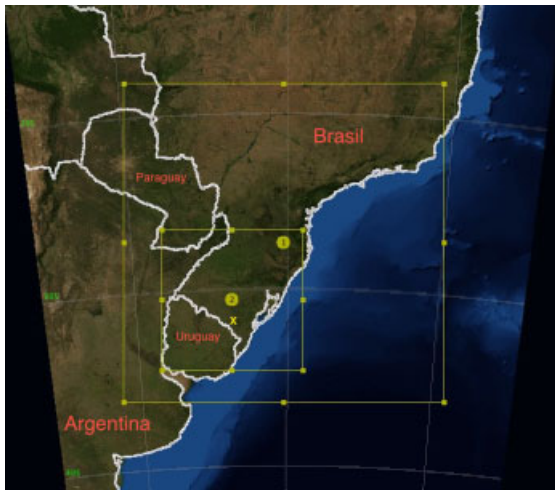


Figure 1. Locations of the outer and inner grids for the WRF mesoscale simulation. The point 'X' marks the location of Candiota. This figure is available in colour online at wileyonlinelibrary.com/journal/met

(Moraes, 2000), allowing the comparison of the results of the present work with observational data obtained in similar meteorological conditions.

The WRF simulation period was from 12 to 15 July 2010, and represents a typical cold air incursion after a cold front passage (Garreaud, 2000). Daily mean meteorological fields from the NCEP/NCAR reanalysis were used to depict the synoptic picture of this event. The synoptic analysis presents a cold front acting over south Brazil during day 12 (not shown), a southeast/northwest oriented cold frontal trough is associated to an extra-tropical cyclone close to the southern South America coast. During day 13, the extra-tropical cyclone and the associated cold front moves offshore. A broad transient high pressure system is present at the frontal region and extends from the north region of Argentina to southern Brazil (not shown). On day 14 (which is the day chosen to be simulated with LES) in southern Brazil there is a west-east oriented ridge associated to the transient high. The counter-clockwise circulation associated with the high promotes the incursion of cold air over the region (Figure 2(a)). The weak pressure gradient drives weak winds at the lower troposphere. Over the continent, westerly

winds weaker than 10 m s^{-1} are observed between the surface and 700 hPa. In Figure 2(b) the Ω field (vertical velocity in the pressure co-ordinate system) and the horizontal wind are shown at 500 hPa. The figure shows a broad region of subsidence over Uruguay and southern Brazil, located at the polar entrance of the upper level subtropical Jet, in agreement with geostrophic theory. Figure 3(a) and (b) show that these synoptic features are also present in the WRF outer domain in this simulation.

The department of Atmospheric Science of the University of Wyoming makes radiosonde data available all over the world through the web. These data may be downloaded at <http://weather.uwyo.edu/upperair/sounding.html>. South American WMO station 83937 (Santa Maria airport) with co-ordinates $(-29.42, -53.41)$ is shown in Figure 1. This corresponds to the point (91, 113) within the WRF inner grid. The comparisons between the WRF output extracted at this point and the Santa Maria soundings (available every 12 h) for the day 14 are reported in Figure 4(a) and (b).

The model is able to capture pretty well the potential temperature (Figure 4(b)) for each of the selected hours. Wind speed profiles (Figure 4(a)) are reproduced slightly worse, as they are generally smoother as compared to the observations. As a consequence, the model misses some features in the wind field, such as a low level jet at about 820 hPa at 1200 Z, day 14, during which WRF underestimates the 850 hPa wind by $7/8 \text{ m s}^{-1}$.

Further experimental data available for the simulated period have been obtained at a meteorological tower that has operated since 2005 at Pedras Altas, a location 30 km south of Candiota $(-31.44, -53.35)$, corresponding to the point (93, 68) of the inner grid. The surface temperature comparison for the whole simulated period between the WRF variable TH2 (potential temperature at 2 m) and the corresponding observations is shown in Figure 5. This comparison shows that the evolution of the surface potential temperature as calculated by WRF (see Table 1) nearly follows that of the observation data during the daytime heating period, while it underestimates the surface temperature by $2-5^\circ \text{C}$ at night time. Recent studies showed that the MYJ PBL scheme dampens the diurnal cycle, with warmer temperatures during cold hours (Ruiz *et al.*, 2010); similarly, a night time warm bias for the Noah LSM scheme under clear-sky conditions has been reported (Miao *et al.*, 2007). However, here

Table 2. WRF setup: grid parameters.

Domain	(N_x, N_y)	(dx, dy) km	(lat, lon) centre point	Eta levels	Y : M : D : H start-end
outer	101,101	20	$(-27.3^\circ, -50.2^\circ)$	50	2010 : 07 : 12 : 00–2010 : 07 : 15 : 23
inner	176,176	5	$(-30.5^\circ, -53.6^\circ)$	50	2010 : 07 : 12 : 00–2010 : 07 : 15 : 23

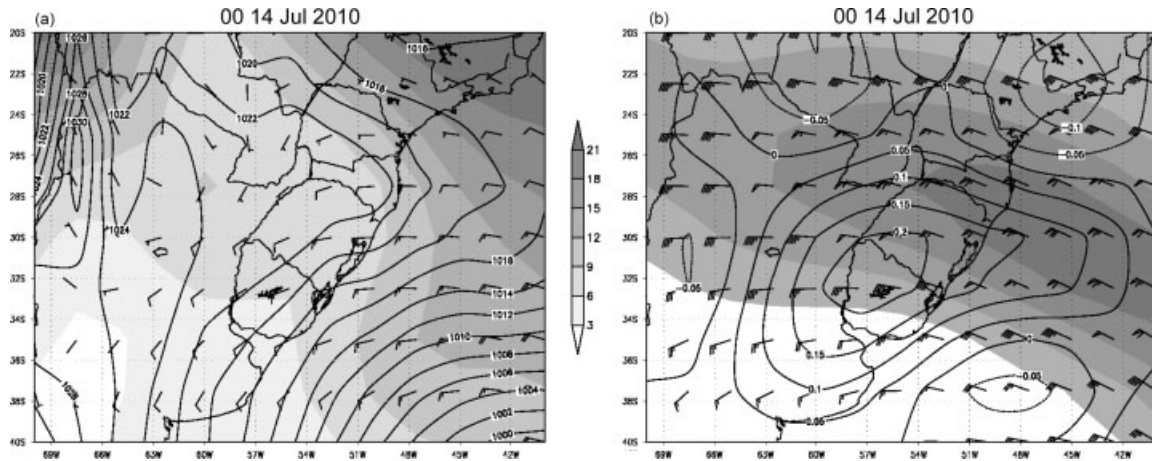


Figure 2. (a) NCEP reanalysis: daily average of mean sea level pressure (black solid lines, hPa), of mean wind in the layer between 1000 and 700 hPa (barbs, m s^{-1}) and of 1000 hPa temperature field (shaded, $^{\circ}\text{C}$); (b) NCEP reanalysis: daily average of 200 hPa wind field (barbs, shaded) indicate the wind magnitude, (m s^{-1}) and of the Ω field (lines, Pa s^{-1}). The black square marks the location of Candiota.

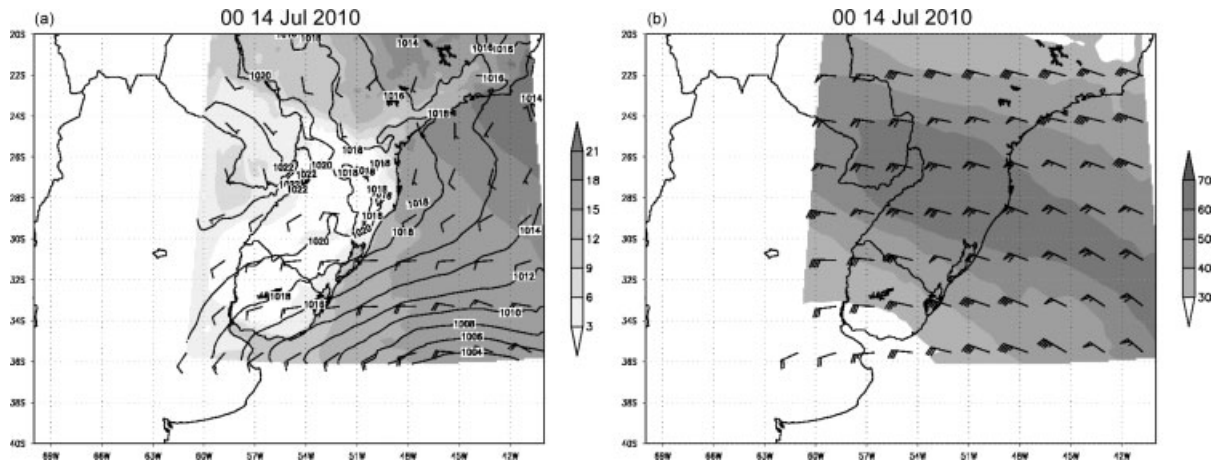


Figure 3. (a) WRF prediction: daily average of mean sea level pressure (black solid lines, hPa), of mean wind in the layer between 1000 and 700 hPa (barbs, m s^{-1}) and of 1000 hPa temperature field (shaded, $^{\circ}\text{C}$); (b) WRF prediction: daily average of 200 hPa wind field (barbs, shaded) indicate the wind magnitude, m s^{-1} and of vertical velocity.

the topic of concern is the daytime heating period of day 14, when the WRF estimation of the potential surface temperature, that influences directly the surface sensible heat flux, is rather good.

3. The large-eddy model

In the present work, the NCAR large-eddy model (Moeng, 1984; Sullivan *et al.*, 1994) is used. It uses the incompressible Boussinesq form of the Navier–Stokes equations and it considers a horizontally homogeneous boundary layer. The PBL variables are spatially filtered to define resolved and subfilter scale (SFS) components. In order to highlight the role of the geostrophic wind we report only the momentum equations for the resolved horizontal components:

$$\begin{aligned} \frac{\partial \bar{u}}{\partial t} &= \overline{u\zeta_z} - \overline{w\zeta_y} + f\bar{v} - \frac{\partial P^*}{\partial x} - \frac{\partial \langle \bar{p} \rangle}{\partial x} \\ &\quad - \left(\frac{\partial \tau_{xx}}{\partial x} + \frac{\partial \tau_{xy}}{\partial y} + \frac{\partial \tau_{xz}}{\partial z} \right) \\ \frac{\partial \bar{v}}{\partial t} &= \overline{w\zeta_x} - \overline{u\zeta_z} - f\bar{u} - \frac{\partial P^*}{\partial y} - \frac{\partial \langle \bar{p} \rangle}{\partial y} \end{aligned} \quad (1)$$

$$- \left(\frac{\partial \tau_{xy}}{\partial x} + \frac{\partial \tau_{yy}}{\partial y} + \frac{\partial \tau_{yz}}{\partial z} \right) \quad (2)$$

where $(\zeta_x, \zeta_y, \zeta_z)$ are the three vorticity components (the advective terms are written in rotational form), the τ are the Reynolds stresses components, g is the gravitational acceleration and f is the Coriolis parameter. The mean horizontal pressure gradient force term ($\langle \bar{p} \rangle$) is written separately so it can be treated as an external forcing, that is:

$$\begin{aligned} \frac{\partial \langle \bar{p} \rangle}{\partial x} &= -fV_g \\ \frac{\partial \langle \bar{p} \rangle}{\partial y} &= fU_g \end{aligned} \quad (3)$$

Here the geostrophic wind components (U_g, V_g) represent the external forcing related to the horizontal gradient of the large-scale pressure fields.

The relation between the SFS fluxes and the resolved-scale velocity field is given by:

$$\tau_{ij} = -K_M \left(\frac{\partial \bar{u}_i}{\partial x_j} + \frac{\partial \bar{u}_j}{\partial x_i} \right), \quad (4)$$

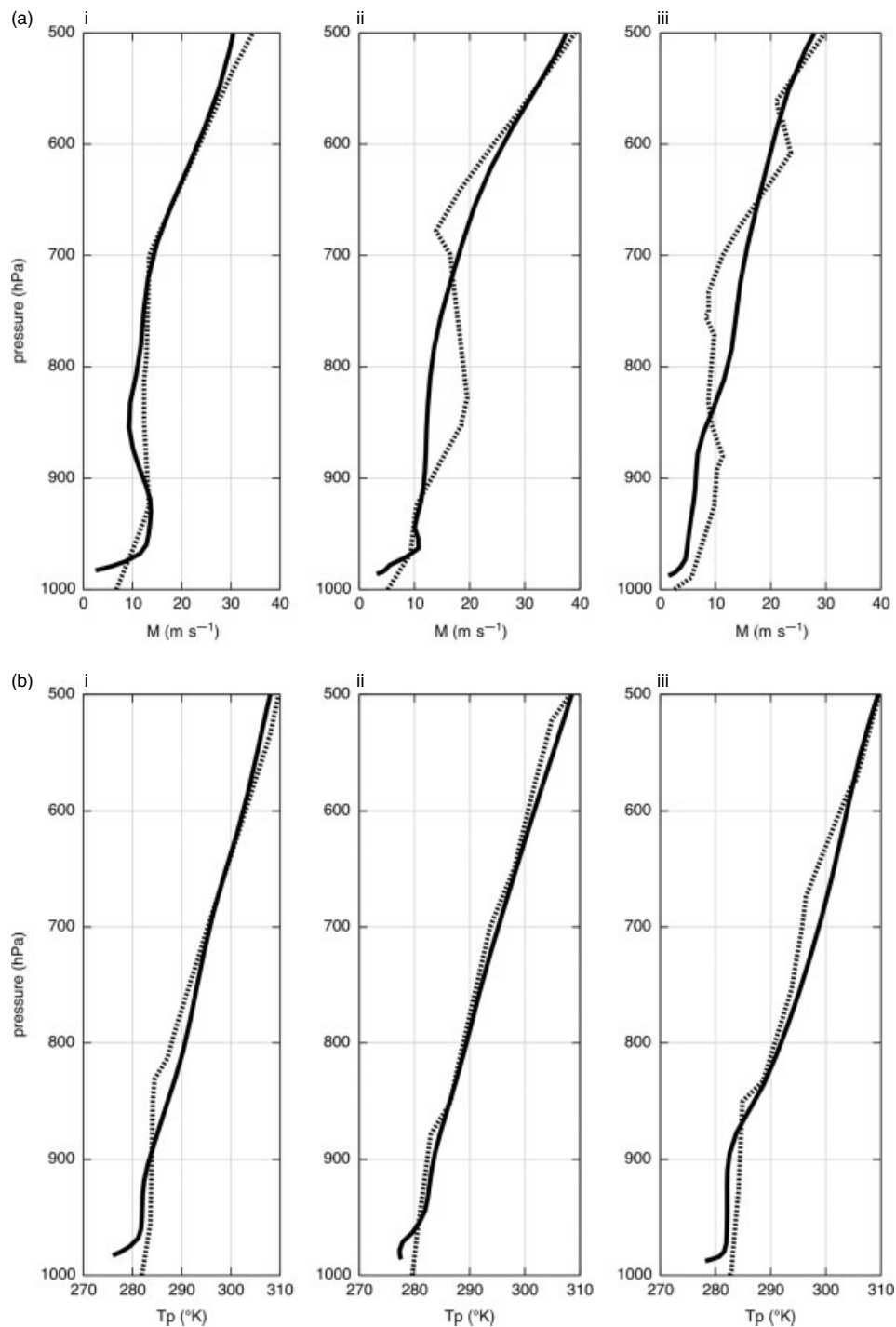


Figure 4. Vertical profiles of (a) the wind speed and (b) the potential temperature taken during day 14 at 0000 Z (i), 1200 Z (ii), and 0000 Z for day 15 (iii). Solid line corresponds to WRF output and dashed line to the sounding data of University of Wyoming.

where $(i, j) = (x, y, z)$, and the eddy viscosity coefficient for the momentum K_M is given by:

$$K_M = 0.1\ell(\overline{e})^{1/2}, \quad (5)$$

where ℓ is the mixing length and $(\overline{e})^{1/2}$ is a velocity scale derived from the SFS energy. The mixing length is calculated as $\ell = \min(kz, \Delta)$ with $\Delta^3 = \frac{2}{3}\Delta_x\frac{2}{3}\Delta_y\frac{2}{3}\Delta_z$. This means that an adjustment in the length scale close to the bounding surface is included if the mixing length exceeds the value obtained from the similarity theory, i.e. kz , where k is the von Karman constant

and z is the height above ground. The boundary conditions in the horizontal were periodic, the upper boundary was specified as a frictionless rigid lid with zero mass, momentum, heat and subgrid kinetic energy fluxes, and the bottom boundary employed a no-slip condition with a prescribed roughness length. Full details of the present LES model including the SFS modelling for the heat flux can be found in Moeng (1984) and Sullivan *et al.* (1994).

It is important to point out that this LES model has been widely used and tested to investigate basic boundary-layer flows (see, e.g., Moeng, 1984; Moeng and Wyngaard, 1988; Moeng

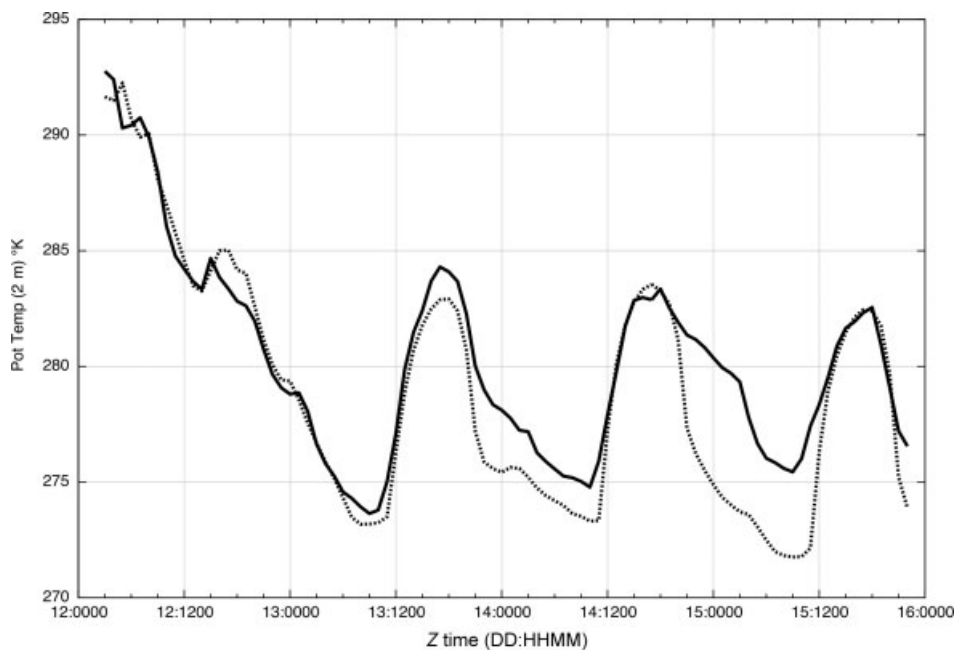


Figure 5. Temporal evolution of the surface potential temperature during the simulated period. The solid line represents the measured surface temperature at Pedras Altas and the dotted lines the output of WRF at the same location.

and Sullivan, 1994; Saiki *et al.*, 2000; Antonelli *et al.*, 2003; Sullivan *et al.*, 2003; Anfossi *et al.*, 2006; Degrazia *et al.*, 2009; Rizza *et al.*, 2010).

4. The case study

4.1. LES numerical setup

The LES domain is localized around the city of Candiota (RS, Brasil), located at $(-31.40, -53.70)$ that corresponds to the point of co-ordinate $(x, y) = (35, 28)$ of the outer WRF grid (Figure 1). The region around Candiota is the South American lowlands or Pampa, in which the dominant vegetation types are grassy prairie. Homogeneous surface fluxes are assumed within the LES domain that has a horizontal extension of 5×5 km.

Typical initialization of LES with idealized atmospheric profiles usually involves a barotropic PBL and the surface heat flux is held constant during the simulation. Realistic settings should include a variation of the surface heat flux that reflects the intensity of the solar heating during the course of the day, the variation of wind intensity with height, a baroclinic geostrophic wind profile and possibly the inclusion of large-scale effects obtained either from observation and/or mesoscale model. All of these aspects have been considered in the investigation.

In Table 3 the LES settings employed for the simulations described in this work are reported. The horizontal domain has an extension of 5×5 km with 128^2 grid points. The vertical extension is 3 km with 192 grid points. The corresponding grid cell resolution is $39 \times 39 \times 15.625$ m that is appropriate for LES under convective conditions. Concerning the geostrophic forcing two different setups are employed. The first (BCL) uses a baroclinic geostrophic wind profile and the second (BTP) the more common barotropic geostrophic profile. The methodology used for the calculation of the baroclinic/barotropic profiles is discussed below.

Table 3. LES settings.

	BCL	BTP
Domain extension	$5 \times 5 \times 3$ km ³	$5 \times 5 \times 3$ km ³
(lat,lon) centre point	$(-31.4, -53.4)$	$(-31.4, -53.4)$
Grid points	$128 \times 128 \times 192$	$128 \times 128 \times 192$
Starting time	14 July 2010: 10Z	14 July 2010: 10Z
Geostrophic wind	Baroclinic	Barotropic (800 hPa)
Surface forcing	(T_2, Q_2)	(T_2, Q_2)
Coriolis parameter	-0.75×10^{-4}	-0.75×10^{-4}

4.2. Initial profiles

The initial data for both LES runs were extracted in the point of coordinate $(-31.40, -53.70)$ of the inner WRF grid and shown in Figure 6. This figure shows the initial profiles of potential temperature (Figure 6(a)), specific humidity (Figure 6(b)) and the (U, V) components of wind field (Figure 6(c) and(d)). The asterisks correspond to the output of WRF model in the lowest 3000 m (19 vertical levels), and the continuous lines represent the linear interpolation over the 192 vertical points in the LES grid. These profiles are taken at 1000 Z, which corresponds to the 0700 am (Z time is equal to UTC-3 h LST) of the 14 July 2010, the starting time of the LES runs. The positive values for both components of wind speed indicate a direction of wind from the southeast. The potential temperature profile is typical of early morning stable conditions, just before the surface warm up and begins to transfer heat to the boundary layer. The initial profile of the specific humidity shows a maximum a few hundred of metres above the surface that decreases with height. It may be noticed that the surface temperature is close to 0°C and the low values for the specific humidity (<3.8 g kg⁻¹), revealing a dry and cold PBL. The U -component is almost 0 near the ground but grows in the lowest 100 m to about 10 m s⁻¹ and from 13 to 22 m s⁻¹ in the layer from 1500 to 3000 m. Similarly, the V -component has an abrupt change from negative to positive values (about

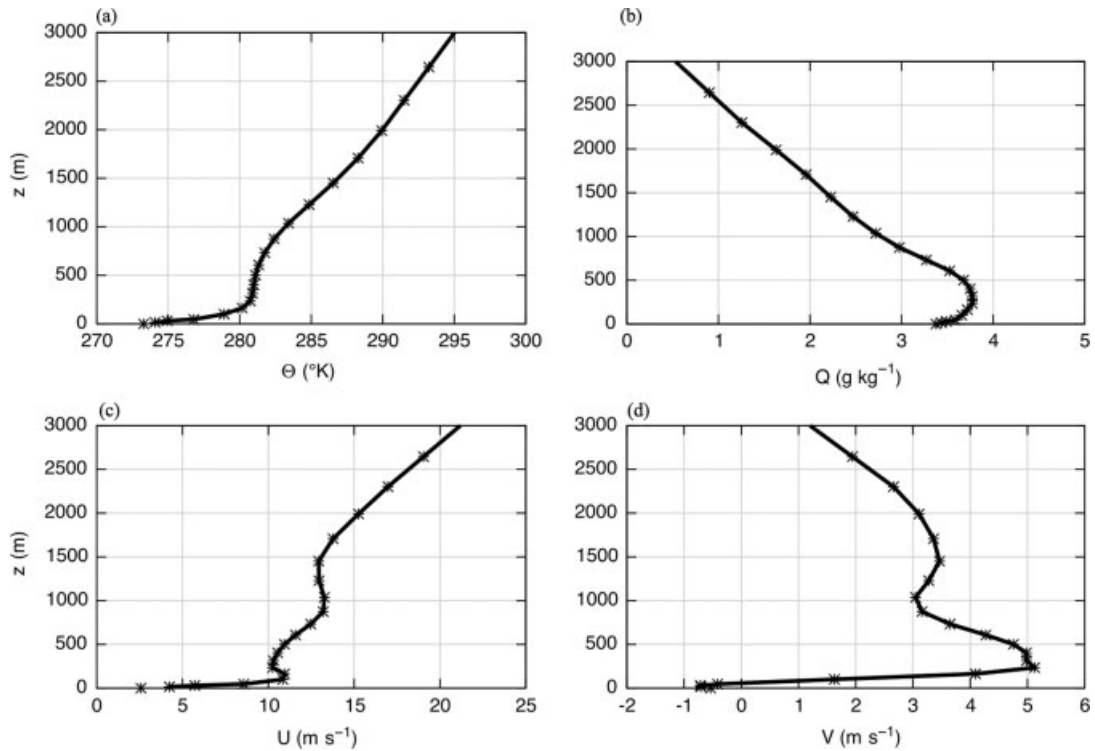


Figure 6. Initial setup of the LES runs. Potential temperature (a), specific humidity (b), longitudinal (c) and lateral (d) components of wind speed. Asterisks correspond to WRF output and continuous line the linear interpolation.

5 m s⁻¹) in the lowest levels, then progressively weakens with height up to about +1 m s⁻¹ at an height of 3000 m.

4.3. Surface forcing

Typically, PBL flows are driven by an imposed surface heat flux and a large-scale horizontal pressure gradient.

The surface sensible heat flux is calculated within the LES code employing the following expression:

$$\overline{\langle w'\theta' \rangle}_{\text{surface}} = \frac{u_* k [\theta_2 - \theta_{z_1}]}{\ln(z_1/2) - \Psi_H(z_1/L)}$$

where θ_2 is the potential temperature at 2 m that is provided by the WRF output variable TH2 and θ_{z_1} is the potential temperature in the first vertical level of the LES grid ($z_1 = 15.625$ m) and $\Psi_H(z)$ is the stability function given by Paulson (1970).

Figure 7 shows the evolution of sensible surface heat flux during the course of day 14. The maximum of this heat flux occurs at 1600 Z (0100 local time) with a value of 0.1 m s⁻¹K in kinematic units. The first point is a very small unrealistic minimum that can be associated with the so-called spin-off time of LES. The zero heat flux occurs at 1900 Z (0400 local time). These results are in agreement with the average winter time sensible heat flux measured at the same location by Moraes (2000). He obtained a peak mean value of 100 W m⁻² that corresponds to 0.1 m s⁻¹K at 1 pm local time and the zero heat flux between 1600 and 1700 local time.

4.4. Geostrophic forcing

The large-scale pressure gradient can be related to the components of the geostrophic wind (U_g , V_g) through Equation (3). Assuming geostrophic balance, the geostrophic wind

components (U_g , V_g) on a constant-pressure surface are given by:

$$\begin{aligned} U_g &= -\frac{f}{g} \frac{\partial Z_p}{\partial y} \\ V_g &= \frac{f}{g} \frac{\partial Z_p}{\partial x} \end{aligned} \quad (6)$$

where g is the acceleration due to gravity (9.81 m s⁻²), f is the Coriolis parameter (-0.75×10^{-4} s⁻¹ at -31.40 latitude) and Z_p is the geopotential height of the constant pressure surface. In much of the atmosphere in midlatitudes, the geostrophic winds provide a good approximation (within 10%) to the actual winds. The major exception is the PBL, in which viscous or friction effects become important, and regions of strong curvature exist where accelerations are large.

The geopotential height in WRF is an output variable that may be calculated from the following expression:

$$Z_p = \frac{(\text{PH} + \text{PHB})}{g} \quad (7)$$

where PH is the perturbation geopotential (m² s⁻²) and PHB is the base-state geopotential (m² s⁻²).

The geostrophic wind profile used within the LES is calculated from the 9 closest points in the outer WRF grid. In this context, the 3 × 3 quadrangle depicted in Figure 8 (the central point P22 corresponds to the city of Candiota) that is used to calculate the horizontal geopotential gradients has a greater extension (40 × 40) km in the outer grid. The geostrophic forcing within the LES is applied until the upper limit of the vertical domain (3000 m). The frequency of the forcing is 1 h

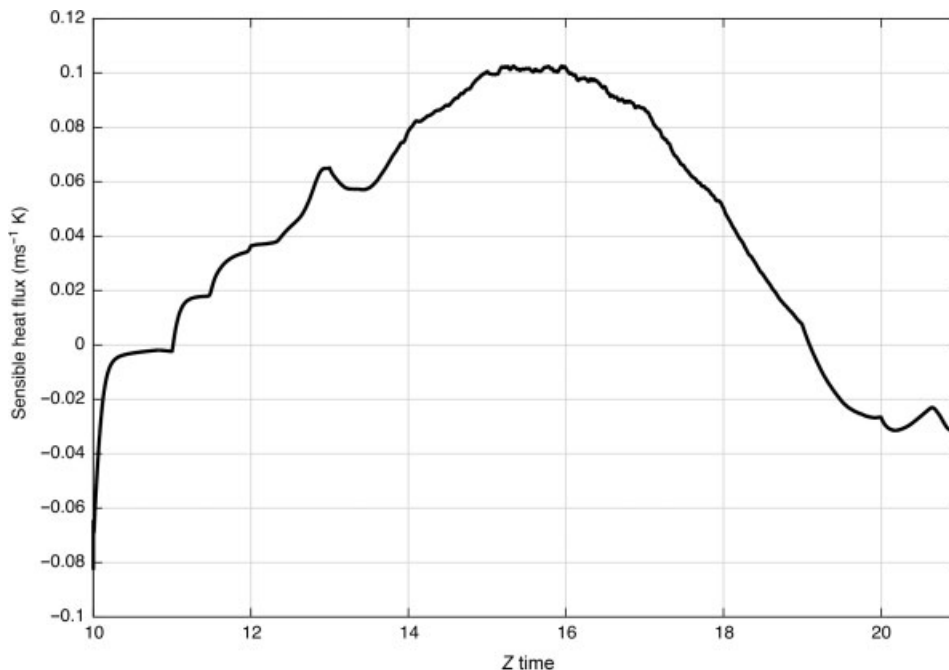


Figure 7. Time plot of surface sensible heat flux as calculated by LES during day 14.

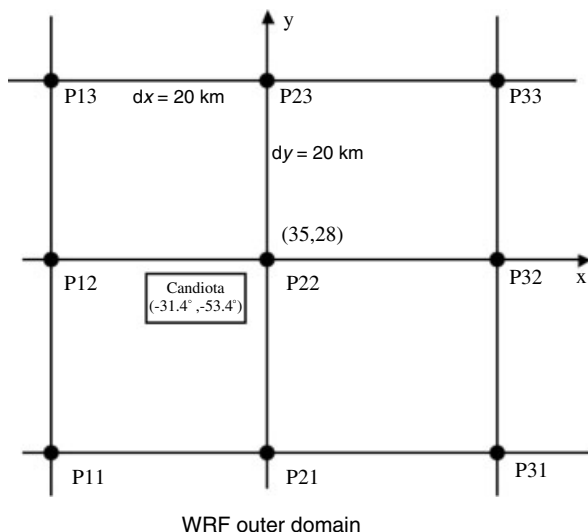


Figure 8. Localization of the city of Candiotia within the WRF outer domain (Point P22).

in correspondence of the frequency of the WRF output fields. This coupling corresponds to a one-way nesting between WRF and LES. The vertical profile of the geostrophic wind is calculated by means of Equation (6). It is first computed in selected isobaric levels then it is transformed in Cartesian vertical coordinates and ingested within the LES domain. In detail the following procedure is adopted:

1. by means Equation (7) the geopotential height is calculated in each ETA-level (50) and for each point of the (3 × 3) quadrangle;
2. extrapolation of the geopotential height in 30 selected isobaric levels (p_i) for each point of the (3 × 3) quadrangle;
3. in each of the p_i isobaric levels, the horizontal derivative is calculated utilizing the classical 3-points formula, and,

4. ingestion of ($U_g(p_i), V_g(p_i)$) into the LES grid, that is to obtain finally ($U_g(z), V_g(z)$).

Figure 9 shows the vertical profile of the magnitude of the actual (extracted from the outer domain at point P22) and geostrophic wind calculated with the above-described steps 1–3 at 1000 Z, 1500 Z and 1800 Z respectively.

The minimum level pressure level of 970 hPa was imposed to avoid unstable gradients of the geopotential close the surface. This figure reveals also that in the range 900:700 hPa the horizontal mean wind is driven essentially by the large scale horizontal pressure gradient. Above 700 hPa an ageostrophic mean wind is evident, which may be caused by the subsidence generated by the transversal polar jet circulation.

Figure 10 depicts the height-time plot of the geostrophic wind components. It is obtained after the calculation described by the above procedure (steps 1–4) and the following temporal interpolation along the time steps of LES.

The U-wind component is maximum and almost constant at upper levels, while in the lower levels it strongly weakens from morning to night-time. The V-component is weaker, the maximum is near the ground at around 12 local time but the diurnal variations are relatively weak.

The barotropic wind shear as used by the simulation (BTP) is obtained by extrapolating the value of the corresponding baroclinic profiles at 800 hPa. This level corresponds to the pressure at 2 km above ground level. As may be seen in Figure 11 the U_g components oscillate around a mean value of 10 m s^{-1} during the simulation period, while V_g oscillates around the mean value of 2 m s^{-1} during the same period.

Finally, to check if the methodology just described provides valuable results the non-dimensional baroclinicity shear parameter has been estimated. It is calculated according to Grant and Whiteford (1987) from the magnitude of the geostrophic shear vector normalized by u_*/h , that is:

$$M(z) = \frac{h}{u_*} \left(\left(\frac{\partial U_g}{\partial z} \right)^2 + \left(\frac{\partial V_g}{\partial z} \right)^2 \right)^{1/2} \quad (8)$$

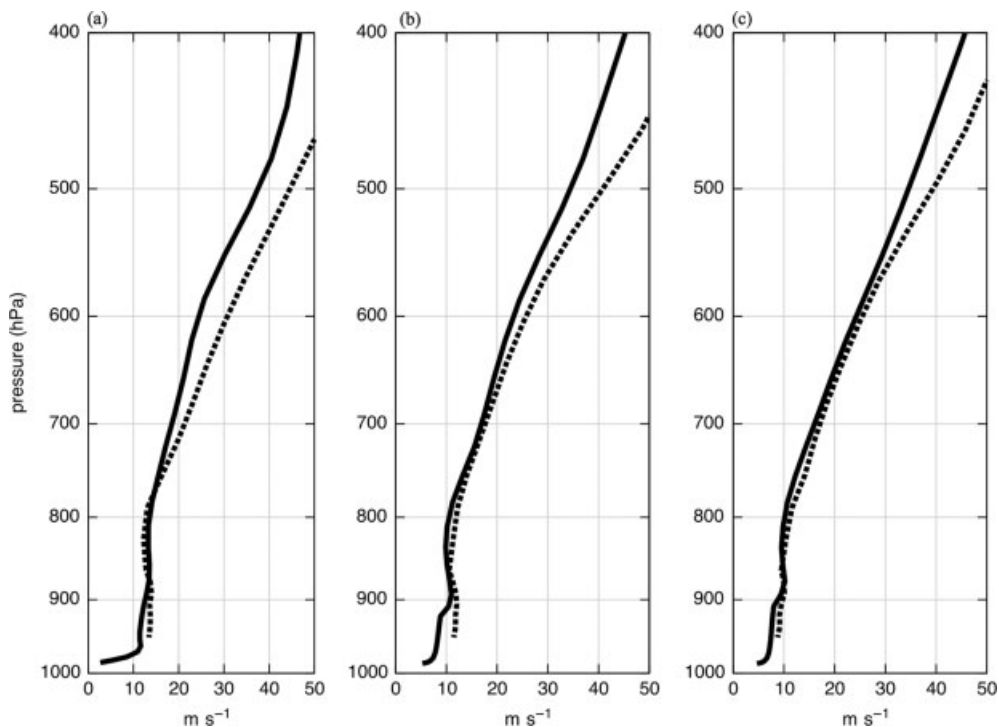


Figure 9. Vertical wind profile at 1000 Z (a), 1500 Z (b) and 1800 Z of day 14 (c). The continuous line represents the magnitude of the WRF horizontal wind components $M = (U^2 + V^2)^{1/2}$, and the dotted line the magnitude of geostrophic wind $G = (U_g^2 + V_g^2)^{1/2}$.

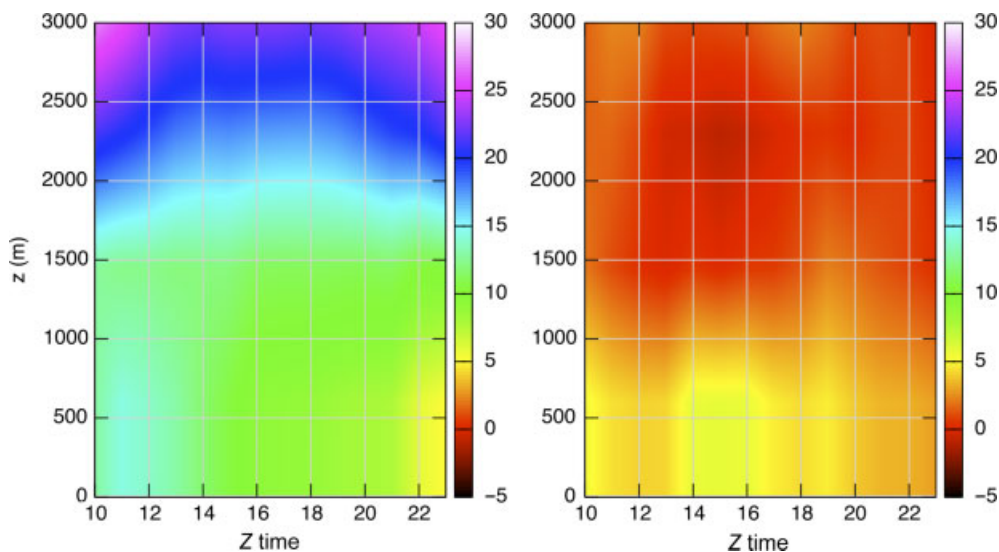


Figure 10. Time-height plot of the components of the geostrophic wind as used by the LES-BCL run. This figure is available in colour online at wileyonlinelibrary.com/journal/met

Figure 12(a) shows the temporal sequence of the vertical integrated baroclinicity parameter that is denoted by $\langle M \rangle$. Figure 12(b) depicts the geostrophic shear components ($S_x = \partial U_g / \partial z$; $S_y = \partial V_g / \partial z$) again computed like a vertical average and denoted by $\langle S_x \rangle$ and $\langle S_y \rangle$. The value of geostrophic shear components is of order 0.005 and 0.0015 for $\langle S_x \rangle$ and $\langle S_y \rangle$, respectively, during the course of the day. The corresponding value of $\langle M \rangle$ is about 8. These values are in agreement with Grant and Whiteford (1987) that found a value of M in the range 2.9–13.7 with a mean value of 7.5 during flights from KONTUR experiment in the North Sea. It may be noticed that the baroclinicity shear parameter begins to grow

in the late afternoon hours, that is during the transition regime before the formation of the stable PBL. This is in agreement with the results of Brown (1996) that using a baroclinic LES reached a value of M between 9.2 and 13.7 for neutral runs.

5. Results and discussion

5.1. Comparison of surface values

Two LES runs were performed from 1000 Z to 2300 Z on 14 July, forced with the methodology described above and reported in Table 3. During this period the PBL stability

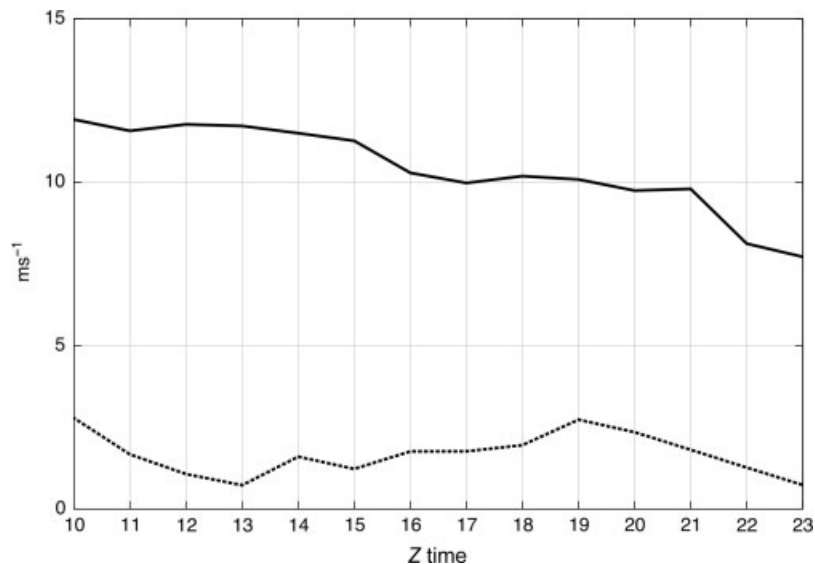


Figure 11. Time plot of the component of the 800 hPa geostrophic wind as used by the LES-BTP run.

conditions ranged from nearly-neutral at the starting time becoming convective during the course of the afternoon and stable after 2000 Z.

In Figure 13(a) the evolution of the friction velocity is reported, as predicted by the surface layer scheme of WRF (solid line) and by the two LES runs, BTP (thin dotted line) and BCL (thick dotted line). It may be seen that in general there is a good agreement between the two LES runs and the WRF estimation of this parameter. In particular, looking at the diurnal cycle it seems that the LES-BCL and the WRF estimations show similar patterns. Moraes (2000) found that for the same location, the average winter time friction velocity daily cycle reaches a maximum of 0.55 m s^{-1} just before noon, decreasing shortly after that and becoming 0.4 m s^{-1} towards the end of the afternoon. Both WRF and the BCL-LES runs show similar evolutions, while the BTP-LES is slightly less turbulent.

Figure 13(b) shows the comparison of the stability parameter h/L , which is a combination of the mixing layer height (h) and the Monin-Obukhov length (L). It is important to point out that the calculation of the PBL height in LES for convective conditions is based on the minimum of the heat flux profile, while WRF uses the MYJ-PBL scheme where the PBL height is defined as the lowest model level above the surface at which the equilibrium turbulent energy becomes negative, or alternatively, as the height of the lowest model level at which TKE approaches its prescribed lower bound (Janjić, 2001).

In all cases, the stability parameter shows that buoyancy effects are expected to dominate over shear effects throughout most of the boundary layer between 1300 Z and 1800 Z corresponding to values of h/L comprised between $[-5, -10]$. These features are more pronounced in the WRF and in BTP-LES runs. On the contrary shear effects are dominant during the transition from convective to stable regimes that is between 1800 Z and 2000 Z.

5.2. Comparisons of vertical profiles

Figure 14(a–d) shows the comparison between the two LES runs of the heat flux profile. At 1100 Z (Figure 14(a)) the heat flux is almost zero with a low negative peak close to ground, indicating stable condition close to ground and a neutral residual PBL above 200 m. At 1700 Z (Figure 14(b)) the heat

flux has a linear profile until 1000 m for both simulations, indicating the development of a convective regime. The heat flux profile at 1900 Z (Figure 14(c)) indicates that the PBL is in a transition phase towards the neutral regime that is attained at 2000 Z (Figure 14(d)).

It is important to perceive that only at the end of the afternoon the heat flux profiles show significant difference between the BTP and BCL runs, originated by an earlier onset of the early evening transition in the BCL case. It may be understood as a consequence of the larger turbulent intensities in the baroclinic case at the end of afternoon (shown as u_* in Figure 13(a)). In the more turbulent BCL case, therefore, the surface cooling is more easily transported upward, driving an earlier evening transition.

In the next two figures the vertical profiles of the specific humidity and virtual potential temperature are reported. The snapshots are taken at 1100 Z (0800 am local time), that is 1 h after the start of the LES runs, at 1500 Z and 1800 Z that is during the development of the convective PBL and finally at 2200 Z that is during the transition towards the stable nocturnal PBL. The LES profiles are obtained by averaging local values in any horizontal plane, while the vertical profiles of WRF are extracted in proximity to the point P22 (see Figure 8) of the inner grid.

The vertical distribution of specific humidity in the PBL depends on the moisture content of the surface, advection of moisture and local sources associated with phase changes of water. The modelled sequence of specific humidity profiles from the simulations is shown in Figure 15(a–d). This figure shows the comparison between the WRF prediction with the LES-BCL and LES-BTP runs at the above-mentioned instants of time.

In general, it may be noticed an overall low value of specific humidity with maximum below $5 \text{ g} \times \text{kg}^{-1}$ indicating rather dry simulations. When there is little evaporation from the surface, specific humidity profiles are nearly uniform with height in the daytime CBL as depicted by the profiles taken at 1500 Z and 1800 Z. An important feature to be pointed out is that the two LES runs gave approximately the same results. On the other hand, the comparison with WRF is very good at 1100 Z, which is likely caused by the influence of initial conditions, while at a later time it appears that the well mixed convective

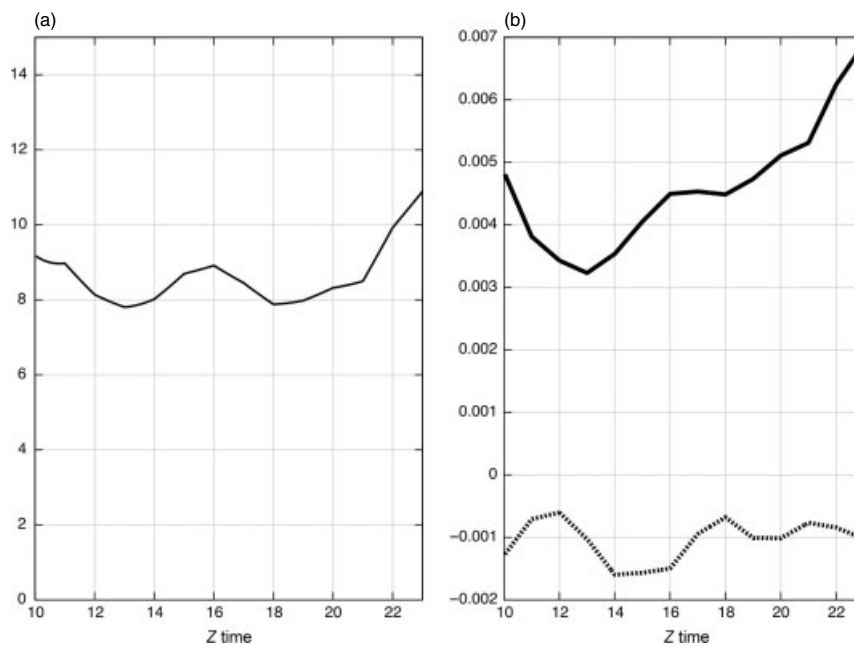


Figure 12. Time plot of the vertical integrated baroclinicity parameter (a) and the geostrophic shear parameters (b).

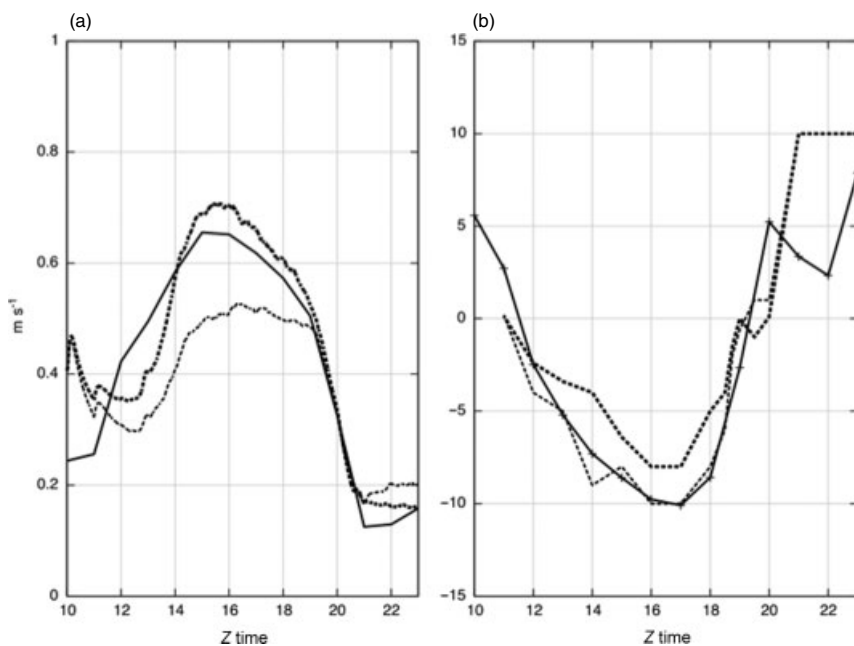


Figure 13. Time plot prediction by LES-BTP (thin dotted line), LES-BCL (thick dotted line) and WRF (solid line) for (a) the friction velocity and (b) the stability parameter h/L .

region in LES is deeper compared with the WRF prediction indicating that the convective motion is better described in LES as a consequence of the highest resolution in the PBL. The BCL run shows a slightly moister PBL, a probable consequence of the more turbulent conditions in that case.

Figure 16(a–d) shows the same temporal sequence for the vertical profile of potential temperature. The potential temperature profile is insensitive to the LES setup, as both BCL and BTP conditions have identical evolutions. It reflects the fact that no temperature advection was considered in the BCL run, a condition supported by the results from Brown (1996). Nevertheless, it is interesting to point out that the most intense turbulence in the BCL case has absolutely no

role in generating the potential temperature profiles, while it causes slightly increased specific humidity. This result is a consequence of the fact that the latent heat fluxes are quite small, and, therefore, are potentially more vulnerable to the surface turbulence. Being fairly large, the sensible heat fluxes do not show the same dependence. This is the most important result of this work. In fact, the intensity of turbulence in the two cases is different. This difference is the phenomenon responsible for all the other variations in the quantities that we have analysed above.

Figure 17(a–d) shows the temporal sequence of the vertical profile of the wind speed magnitude $(U^2 + V^2)^{1/2}$. At 1100 Z (Figure 17(a)) as it can be easily observed, there is a very good

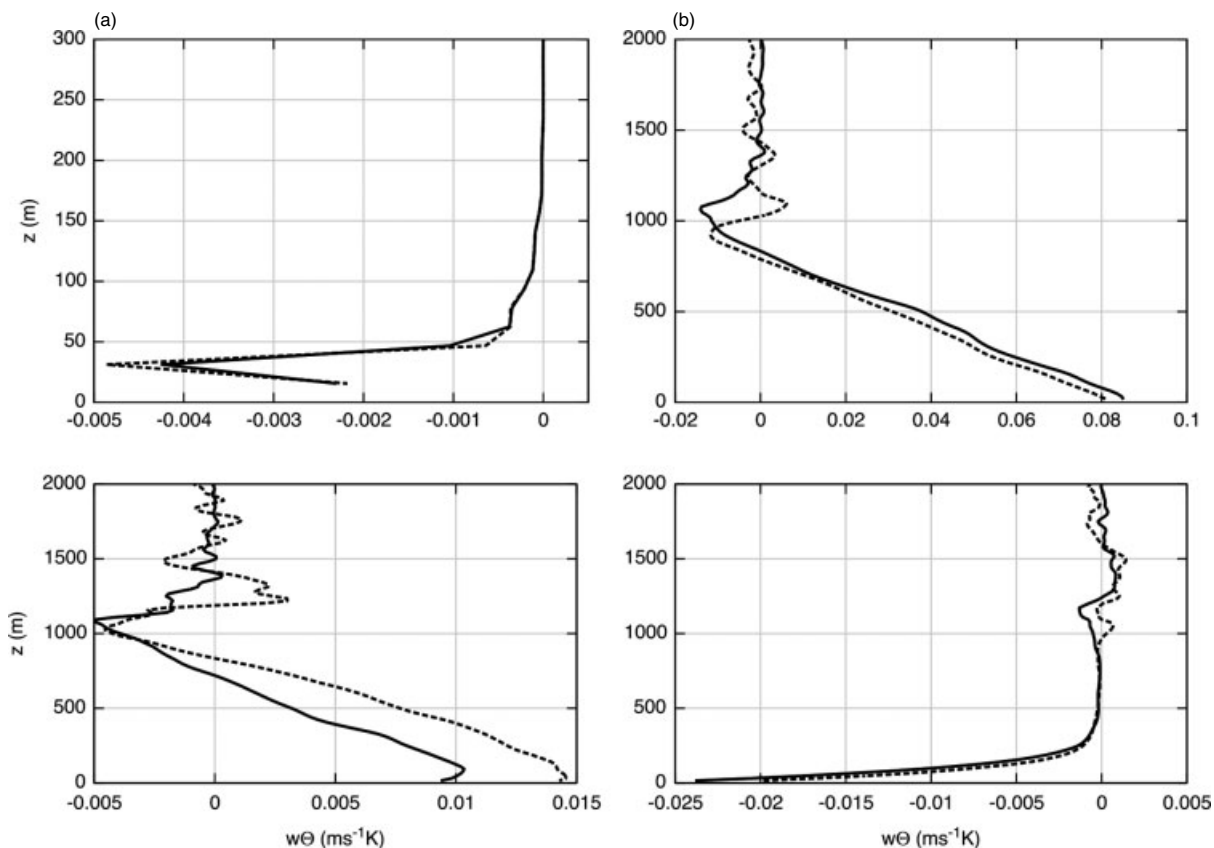


Figure 14. Vertical distribution of the heat flux profiles at 1100 Z (a), 1700 Z (b), 1900 Z (c) and 2200 Z (d), for LES-BCL (solid line) and LES-BTP (dashed line).

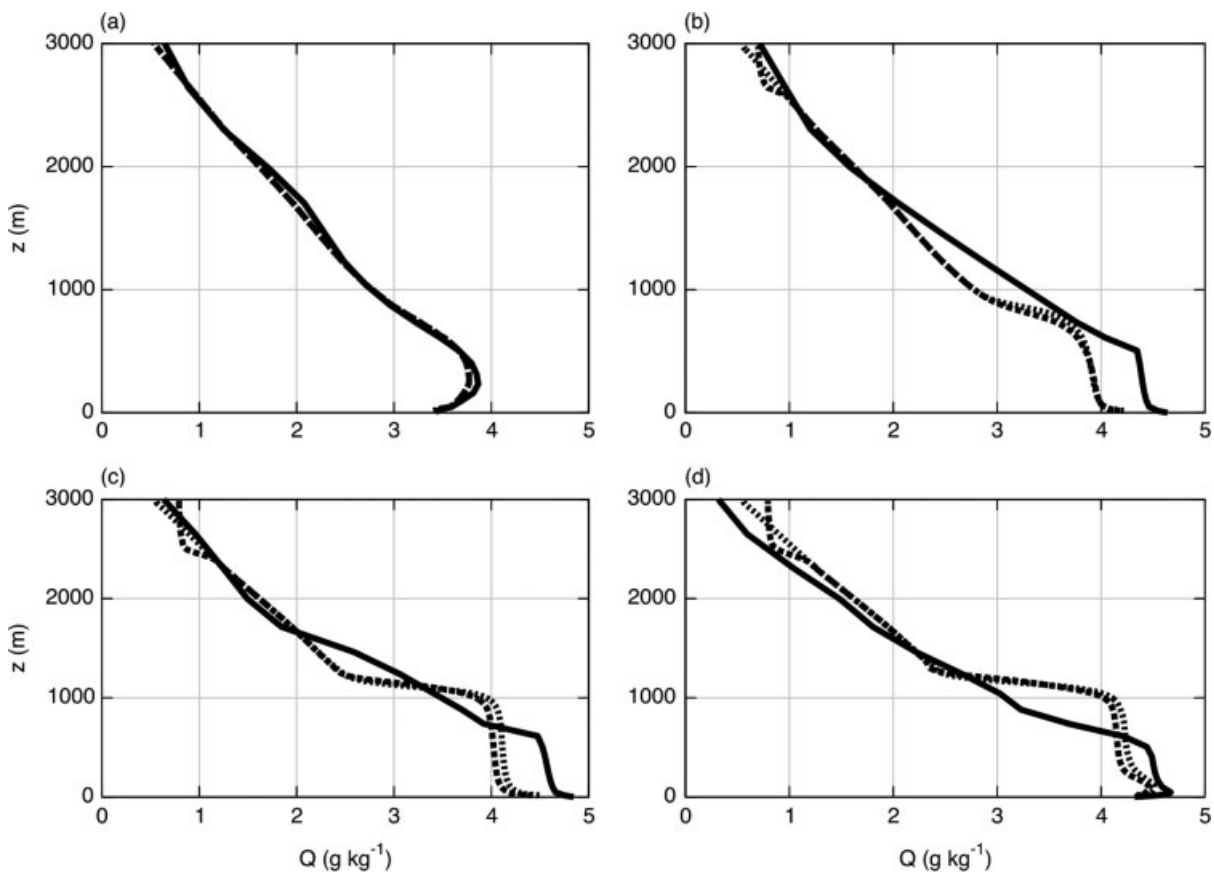


Figure 15. Vertical distribution of the specific humidity at 1100 Z (a), 1700 Z (b), 1900 Z (c) and 2200 Z (d), for LES-BCL (thin dashed line), LES-BTP (thick dashed line) and WRF (solid line).

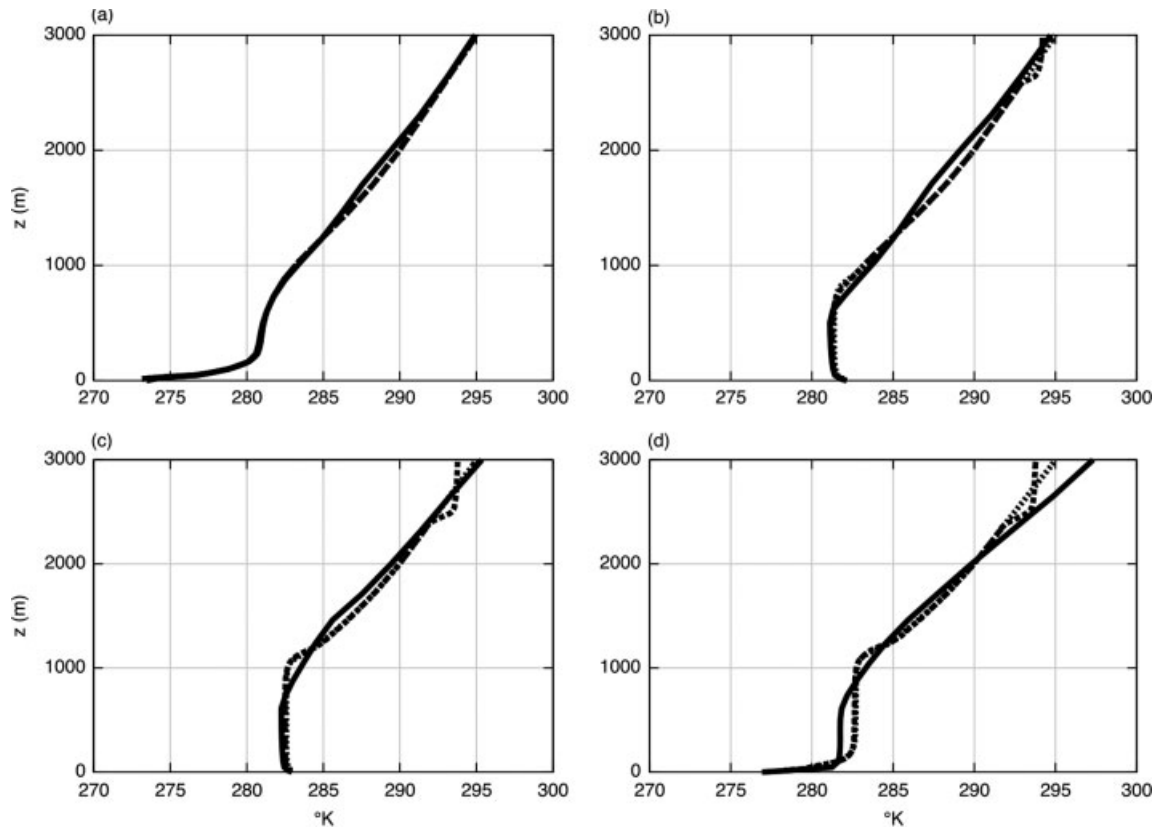


Figure 16. Vertical distribution of the potential temperature at 1100 Z (a), 1700 Z (b), 1900 Z (c) and 2200 Z (d), for LES-BCL (thin dashed line), LES-BTP (thick dashed line) and WRF (solid line).

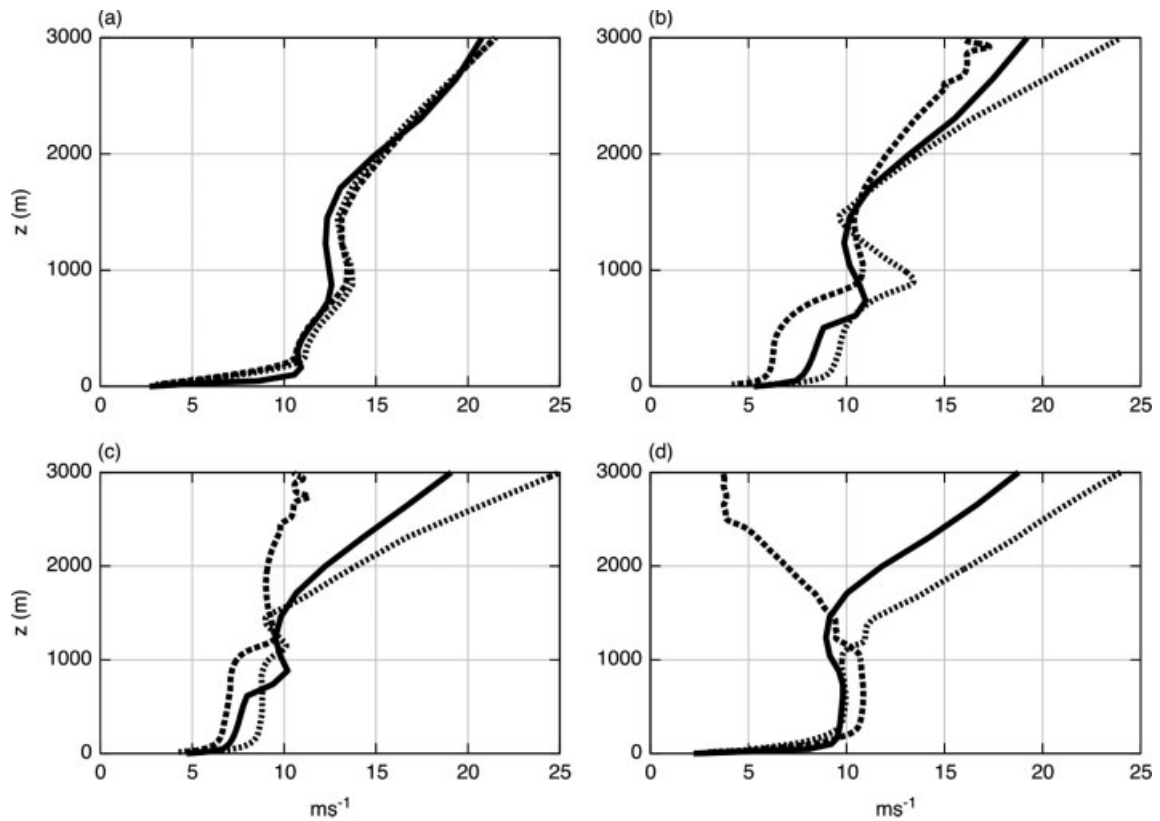


Figure 17. Vertical distribution of the wind speed at 1100 Z (a), 1700 Z (b), 1900 Z (c) and 2200 Z (d), for LES-BCL (thick dashed line), LES-BTP (thin dashed line) and WRF (solid line).

agreement for both LES runs with the corresponding WRF profile. At 1500 Z (Figure 17(b)) the agreement is still good but it can be observed that above 1500 m the LES-BTP begin to decouple with WRF. This decoupling is more evident at 1800 Z (Figure 17(c)) and 2200 Z (Figure 17(d)) profiles. On the other hand, it may be noticed that the LES-BCL simulation is still well correlated with WRF, above 1000 m the difference may be caused by the ageostrophic part of the wind that is perpendicular to the acceleration and directed to the right from it in the Southern Hemisphere. In general, the performed analysis suggests that, when analysing the vertical profiles of virtual potential temperature and specific humidity, the two LES runs gave comparable results between them and with the corresponding WRF profiles. This is in part explained by the fact no extra terms are added to the LES equation to take into account the thermal winds in the baroclinic PBL. On the other hand looking at the vertical profiles of the wind speed magnitude then the LES-BCL produces a better correlation with the corresponding WRF profiles than the LES-BTP. This result in part confirms the importance of the baroclinic setup to simulate wind speed pattern using LES.

It is clear that the final test for LES predictions may be given only by comparing with experimental data. By the way, it should be emphasized that the WRF simulation has been checked at many levels. First, it has been compared against synoptic data (Figure 2(a,b)), then the wind and temperature profiles are compared against UNWY sounding data (Figure 4(a,b)), and finally to local observations of surface potential temperature (Figure 5). The methodology of calculating the geostrophic wind profiles has been compared with literature data of the baroclinic shear parameter (Figure 12) and found a good agreement. Furthermore, the LES prediction of friction velocity and surface sensible heat flux has been compared with local climatological data and found a reasonable agreement.

5.3. The late afternoon decay of TKE

This last section is motivated by an important and actual subject concerning sunset turbulence decay. Around sunset, the external forcings such as the upward sensible heat flux and the geostrophic forcing vary very rapidly, hence, in this transitional period an equilibrium no longer exists within the PBL. In this context, the decay of the convective turbulence in the adiabatic remnant of the daytime boundary layer is studied with LES, underlining the role of baroclinicity in this particular situation that happens daily in the PBL at sunset.

In Figure 18, the time-height plot of the total (resolved+subfilter) TKE for the BTP-LES (a) and BCL-LES (b) is shown. It is calculated following Nieuwstadt and Brost (1986) as the horizontal average:

$$\langle \text{TKE} \rangle = \frac{1}{L^2} \int_0^L \int_0^L \text{TKE}(LE + SFS) dx dy \quad (9)$$

where *LE* and *SFS* are respectively the resolved and subfilter components of the kinetic energy. The heating/cooling PBL cycle is evident for both cases. Unlike the BTP-LES, the BCL-LES presents a mid-afternoon TKE maximum close to the ground, associated with the intense wind shear activity, enhanced by baroclinicity. In both cases, TKE decreases sharply at 1800 Z, 2 h after the sensible heat flux maximum and 3 h before it becomes negative.

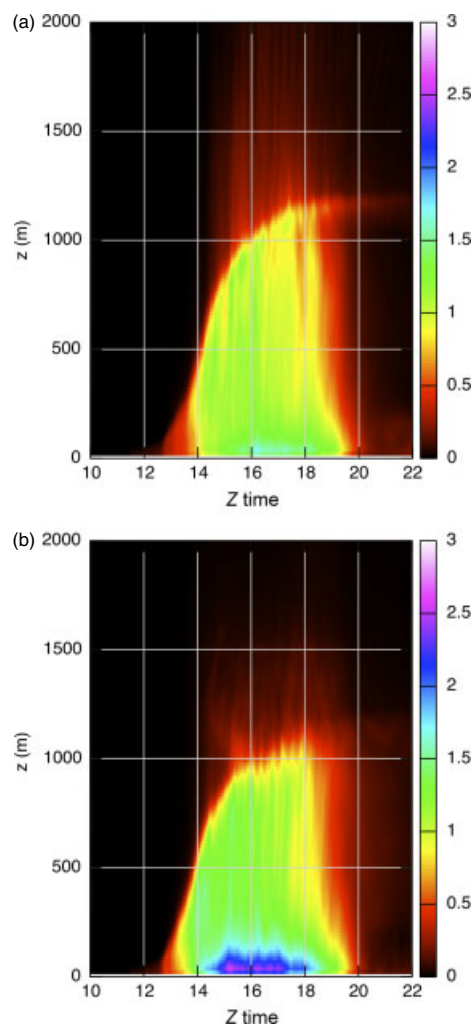


Figure 18. Time height plot of the horizontal average TKE, for LES-BTP (a) and LES-BCL (b). This figure is available in colour online at wileyonlinelibrary.com/journal/met

The temporal evolution around the transition may be analysed by considering the PBL vertically averaged TKE, calculated following Nieuwstadt and Brost (1986) as:

$$[\langle \text{TKE} \rangle] = \frac{1}{h} \int_0^h \langle \text{TKE} \rangle dz. \quad (10)$$

It is a function of the two dimensionless parameters t/t^* and τ_f/t^* , where $t^* = h/w_*$ is the convective time scale, τ_f is the time period over which the surface heat flux decreases from its positive maximum value to zero and w_* is the convective velocity scale. The results are scaled by $w_*(1600Z) = w_{*0} = 1.5 \text{ m s}^{-1}$, $h(1600Z) = h_0 = 1000 \text{ m}$ and $(w'\theta')$ (1600Z) = $0.1 \text{ m s}^{-1}\text{K}$, so that $t^* = 11 \text{ min}$, while $\tau_f = 180 \text{ min}$.

This is equivalent to the intermediate case simulated by Sorbjan (1997), who found, in agreement with Nieuwstadt and Brost (1986) that TKE decays as:

$$\frac{[\langle \text{TKE} \rangle]}{w_{*0}^2} = F\left(\frac{t}{t^*}, \frac{\tau_f}{t^*}\right) \propto (t - t_0)^{-2} \quad (11)$$

In the present study, it is found that Equation (11) is a good representation of the TKE decay for both the LES-BTP and LES-BCL cases. This is in spite of the fact that the mid

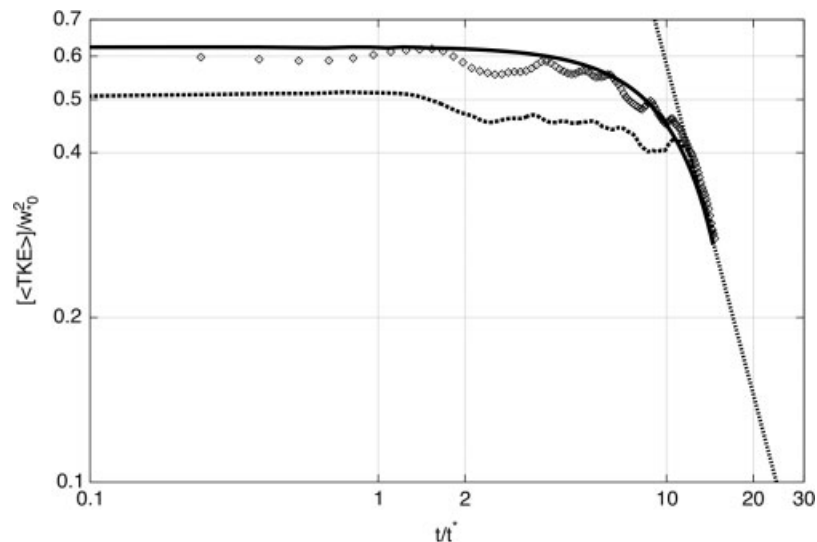


Figure 19. Decay of the TKE for LES-BCL (points) and LES-BTP (thick dashed line). The continuous line represents the analytical model of Goulart *et al.* (2010), the -2 power law (thin dashed line) is also shown for comparison.

afternoon TKE magnitudes are appreciably different in both cases, being larger when it is baroclinic. However, once the transition starts, both curves collapse to a -2 power law, as described by Equation (11). Goulart *et al.* (2010) proposed an analytical expression for the TKE decay considering the wind shear production term. This curve is also displayed in Figure 19, being in close agreement with the LES-BCL results during the afternoon, and also decaying as a -2 power of the dimensionless time during the transition. Furthermore, Goulart *et al.* (2003) found an analytical solution lacking the mechanical shear production term, which has a magnitude closer to the LES-BTP results, and also follows the same decay rate after sunset. These results show that the wind shear obviously affects the afternoon TKE magnitude, but does not interfere with the TKE decaying rate, which seems to be universal, regardless of the turbulent forcing. The decaying rate is further supported by observational evidence provided by Anfossi *et al.* (2004), who found the same power law from TKE measurements following a total solar eclipse in northern France. Our analysis demonstrated that when using a geostrophic wind shear profile, varying with time, the prediction of the magnitude of the TKE decay at sunset were better described when compared with an analytical model of TKE decay. It should be pointed out that the calculation of wind shear vertical profile has been possible with the one-way coupling described in Section 4.4.

6. Conclusions

The present analysis suggests that providing valuable data for initial conditions and updated hourly surface and geostrophic forcing for large eddy simulation (LES) may be useful to allow LES to be prognostic in the investigation of a realistic planetary boundary layer (PBL). Furthermore, in the present work a methodology is described in order to derive the components of the geostrophic wind profile that is used in LES to model the horizontal mean pressure gradient and treated as an external forcing. This methodology involves the mesoscale model WRF directly. In this context, the WRF model has a dual task: (1) providing realistic external forcings to LES and (2) providing a very large dataset to investigate possible improvements for the LES setting to make the numerical prediction more realistic. It

is important to point out that the output of model WRF has been tested accurately against synoptic and local data, and a good agreement found. The principal result obtained by the present study is that the use of geostrophic wind shear profiles improves the prognostic capability of LES in reproducing the wind field pattern in the real PBL. It has been also demonstrated that it is a key ingredient in the description of the decay of the turbulent kinetic energy at sunset.

The natural extension of this preliminary work involves: (1) the inclusion of experimental measured data to initialize the LES runs and also to validate LES with observational data; (2) investigation of the nocturnal stable conditions with possibly a larger LES resolution; (3) an improved methodology to estimate the geostrophic wind speed profile using higher order methods to calculate the horizontal geopotential gradients, and finally (4) the accounting for large-scale temperature advection associated with baroclinicity.

References

- Acevedo OC, Fitzjarrald DR. 2001. The early evening surface-layer transition: temporal and spatial variability. *Journal of the Atmospheric Sciences* **58**: 2650–2667.
- Anderson WC, Basu S, Letchford CW. 2007. Comparison of dynamic subgrid-scale models for simulations of neutrally buoyant shear-driven atmospheric boundary layer flows. *Environmental Fluid Mechanics* **7**: 195–215.
- Andren A, Brown AR, Mason PJ, Graf J, Schumann U, Moeng C-H, Nieuwstadt FTM. 1994. Large-eddy simulation of a neutrally stratified boundary layer: a comparison of four computer codes. *Quarterly Journal of the Royal Meteorological Society* **120**: 1457–1484.
- Anfossi D, Rizza U, Mangia C, Degrazia GA, Marques Filho EP. 2006. Estimation of the ratio between the Lagrangian and Eulerian time scales in an atmospheric boundary layer generated by large eddy simulation. *Atmospheric Environment* **40**: 326–337.
- Anfossi D, Schayes G, Degrazia GA, Goulart A. 2004. Atmospheric turbulence decay during the solar total eclipse of 11 August 1999. *Boundary-Layer Meteorology* **111**: 301–311.
- Antonelli M, Mazzino A, Rizza U. 2003. Statistics of temperature fluctuations in a buoyancy dominated boundary-layer flow simulated by a large-eddy simulation model. *Journal of the Atmospheric Sciences* **60**: 215–224.
- Arya SPS, Wyngaard J. 1975. Effect of baroclinicity on wind profiles and the geostrophic drag law for the convective planetary boundary layer. *Journal of the Atmospheric Sciences* **32**: 767–778.

- Basu S, Vinuesa JF, Swift A. 2008. Dynamic LES modeling of a diurnal cycle. *Journal of Applied Meteorology and Climatology* **47**: 1156–1174.
- Beare RJ, MacVean MK, Holtslag AAM, Cuxhart J, Esau I, Golaz J-C, Jimenez MA, Khairoutdinov M, Kosovich B, Lewellen D, Lund TS, Lundquist JK, McCabe A, Moene AF, Noh Y, Raasch S, Sullivan PP. 2006. An intercomparison of large-eddy simulations of the stable boundary layer. *Boundary-Layer Meteorology* **118**: 247–272.
- Brown AR. 1996. Large-eddy simulation and parametrization of the baroclinic boundary-layer. *Quarterly Journal of the Royal Meteorological Society* **122**: 1779–1798.
- Brown AR. 1999. Large-eddy simulation and parametrization of the effects of shear on the shallow cumulus convection. *Boundary-Layer Meteorology* **91**: 65–80.
- Brown AR, Derbyshire SH, Mason PJ. 1994. Large-eddy simulation of stable atmospheric boundary layers with a revised stochastic subgrid model. *Quarterly Journal of the Royal Meteorological Society* **120**: 1485–1512.
- Chen F, Dudhia J. 2001. Coupling an advanced land surface–hydrology model with the Penn State–NCAR MM5 modeling system. Part II: preliminary model validation. *Monthly Weather Review* **129**: 587–604.
- Clarke RH, Dyer AJ, Brook RR, Reid DJ, Troup AJ. 1971. *The Wangara Experiment: Boundary Layer Data*, Technical Paper 19. Division of Meteorological Physics, CSIRO: Melbourne, Australia.
- Conzemius RJ. 2004. The effects of wind shear on the convective boundary layer entrainment, PhD dissertation, University of Oklahoma, Norman, OK, USA.
- Conzemius RJ, Fedorovich E. 2007. A case study of convective boundary layer development during IHOP: numerical simulations compared to observations. *Monthly Weather Review* **136**: 2305–2320.
- Deardorff JW. 1970. Preliminary results from numerical integrations of the unstable planetary boundary layer. *Journal of the Atmospheric Sciences* **27**: 1209–1211.
- Deardorff JW. 1972. Numerical investigation of neutral and unstable planetary boundary layers. *Journal of the Atmospheric Sciences* **29**: 91–115.
- Deardorff JW. 1980. Stratocumulus-capped mixed layers derived from a three-dimensional model. *Boundary-Layer Meteorology* **18**: 495–527.
- Degrazia GA, Rizza U, Puhales FS, Goulart AG, Carvalho J, Sausen Welter G, Marques Filho EP. 2009. A variable mesh spacing for large-eddy simulation models in the convective boundary layer. *Boundary-Layer Meteorology* **131**: 277–292.
- Garreaud RD. 2000. Cold air incursions over subtropical South America: mean structure and dynamics. *Monthly Weather Review* **128**: 2544–2559.
- Goulart A, Bodmann BEJ, de Vilhena MTMB, Soares PMM, Moreira DM. 2010. On the time evolution of the turbulent kinetic energy spectrum for decaying turbulence in the convective boundary layer. *Boundary-Layer Meteorology* **138**: 61–75.
- Goulart A, Degrazia GA, Rizza U, Anfossi D. 2003. A theoretical model for the study of the convective turbulence decay and comparison with LES data. *Boundary-Layer Meteorology* **107**: 143–155.
- Grant ALM, Whiteford R. 1987. Aircraft estimates of the geostrophic drag coefficient and the rossby similarity functions A and B over the sea. *Boundary-Layer Meteorology* **39**: 219–231.
- Janjić ZI. 2001. *Nonsingular Implementation of the Mellor–Yamada Level 2.5 Scheme in the NCEP Meso Model*, Office Note #437. National Centers for Environmental Prediction: Camp Springs, MD.
- Kosovic B. 1997. Subgrid-scale modelling for the large-eddy simulation of high-Reynolds-number boundary layers. *Journal of Fluid Mechanics* **336**: 151–182.
- Mason PJ. 1989. Large-eddy simulation of the convective atmospheric boundary layer. *Journal of the Atmospheric Sciences* **46**: 1492–1516.
- Mason PJ, Thomson DJ. 1987. Large-eddy simulations of the neutral-stability planetary boundary layer. *Quarterly Journal of the Royal Meteorological Society* **113**: 413–443.
- Mellor GL, Yamada T. 1982. Development of a turbulence closure model for geophysical fluid problems. *Reviews of Geophysics and Space Physics* **20**: 851–875.
- Miao J-F, Chen D, Borne K. 2007. Evaluation and comparison of Noah and Pleim–Xiu land surface models in MM5 using GÖTE2001 data: spatial and temporal variations in near-surface air temperature. *Journal of Applied Meteorology and Climatology* **46**: 1587–1605.
- Moeng C-H. 1984. A large-eddy-simulation model for the study of planetary boundary-layer turbulence. *Journal of the Atmospheric Sciences* **41**: 2052–2062.
- Moeng C-H, Dudhia J, Klemp J, Sullivan PP. 2007. Examining two-way grid nesting for large eddy simulation of the PBL using the WRF model. *Monthly Weather Review* **135**: 2295–2311.
- Moeng C-H, Sullivan PP. 1994. Comparison of shear and buoyancy-driven planetary boundary layer flows. *Journal of the Atmospheric Sciences* **51**: 999–1022.
- Moeng C-H, Wyngaard JC. 1988. Evaluation of turbulent transport and dissipation closures in second-order modelling. *Journal of the Atmospheric Sciences* **46**: 2311–2330.
- Moraes OLL. 2000. Turbulence characteristics in the surface boundary layer over the South American Pampa. *Boundary-Layer Meteorology* **96**: 317–335.
- Nieuwstadt FTM, Brost RA. 1986. The decay of convective turbulence. *Journal of the Atmospheric Sciences* **43**: 532–546.
- Nieuwstadt FTM, Mason PJ, Moeng C-H, Schumann U. 1992. Large-eddy simulation of the convective boundary layer: a comparison of four computer codes. In *Turbulent Shear Flows 8: Selected Papers from the Eighth International Symposium on Turbulent Shear Flows*, Durst F (ed.). Springer-Verlag: Berlin; 343–367.
- Paulson CA. 1970. The mathematical representation of wind and temperature profiles in the unstable atmospheric surface layer. *Journal of Applied Meteorology* **9**: 857–861.
- Pino D, Vilà-Guerau de Arellano J, Duynkerke PG. 2003. The contribution of shear to the evolution of a convective boundary layer. *Journal of the Atmospheric Sciences* **60**: 1913–1926.
- Porté-Agel F, Meneveau C, Parlange MB. 2000. A scale-dependent dynamic model for large-eddy simulations: application to a neutral atmospheric boundary layer. *Journal of Fluid Mechanics* **415**: 261–284.
- Rizza U, Degrazia GA, Mangia C, Marques Filho EP. 2010. Estimation of the Kolmogorov constant for the Lagrangian velocity spectrum and structure function under different PBL stability regimes generated with LES. *Physica A: Statistical Mechanics and its Applications* **389**: 4009–4017.
- Ruiz JJ, Saulo C, Nogués-Paegle J. 2010. WRF model sensitivity to choice of parameterization over South America: validation against surface variables. *Monthly Weather Review* **138**: 3342–3355.
- Saiki EM, Moeng C-H, Sullivan PP. 2000. Large-eddy simulation of the stably stratified planetary boundary layer. *Boundary-Layer Meteorology* **95**: 1–30.
- Scipion D, Palmer R, Chilson P, Fedorovich E, Botnick A. 2009. Retrieval of convective boundary layer wind field statistics from radar profiler measurements in conjunction with large eddy simulation. *Meteorologische Zeitschrift* **18**: 175–187.
- Sorbján Z. 1997. Decay of convective turbulence revisited. *Boundary-Layer Meteorology* **82**: 501–515.
- Sorbján Z. 2004. Large-eddy simulations of the baroclinic mixed layer. *Boundary-Layer Meteorology* **112**: 57–80.
- Stevens B, Moeng C-H, Sullivan PP. 1999. Large-eddy simulations of radiatively driven convection: sensitivities to the representation of small scales. *Journal of the Atmospheric Sciences* **56**: 3963–3984.
- Sullivan PP, Horst TW, Lenschow DH, Moeng C-H, Weil JC. 2003. Structure of subfilter-scale fluxes in the atmospheric surface layer with application to large-eddy simulation modelling. *Journal of Fluid Mechanics* **482**: 101–139.
- Sullivan PP, McWilliams JC, Moeng C-H. 1994. A subgrid model for large-eddy simulation of planetary boundary layer flows. *Boundary-Layer Meteorology* **71**: 247–276.
- Sullivan PP, Moeng C-H, Stevens B, Lenschow DH, Mayor SD. 1998. Structure of the entrainment zone capping the convective atmospheric boundary layer. *Journal of the Atmospheric Sciences* **55**: 3042–3064.
- Zilitinkevich SS, Esau IN. 2003. The effect of baroclinicity on the equilibrium depth of neutral and stable planetary boundary layers. *Quarterly Journal of the Royal Meteorological Society* **129**: 3339–3356.